Advanced Review

The uniform electron gas

Pierre-François Loos* and Peter M. W. Gill

The uniform electron gas or UEG (also known as jellium) is one of the most fundamental models in condensed-matter physics and the cornerstone of the most popular approximation—the local-density approximation—within density-functional theory. In this article, we provide a detailed review on the energetics of the UEG at high, intermediate, and low densities, and in one, two, and three dimensions. We also report the best quantum Monte Carlo and symmetry-broken Hartree-Fock calculations available in the literature for the UEG and discuss the phase diagrams of jellium.

How to cite this article:
WIREs Comput Mol Sci 2016, 6:410–429. doi: 10.1002/wcms.1257

INTRODUCTION

The final decades of the 20th century witnessed a major revolution in solid-state and molecular physics, as the introduction of sophisticated exchange-correlation models[1] propelled density-functional theory (DFT) from qualitative to quantitative usefulness. The apotheosis of this development was probably the award of the 1998 Nobel Prize for Chemistry to Walter Kohn[2] and John Pople[3] but its origins can be traced to the prescient efforts by Thomas, Fermi, and Dirac, more than 70 years earlier, to understand the behavior of ensembles of electrons without explicitly constructing their full wave functions.

In principle, the cornerstone of modern DFT is the Hohenberg–Kohn theorem[4] but, in practice, it rests largely on the presumed similarity between the electronic behavior in a real system and that in the hypothetical three-dimensional (3D) uniform electron gas (UEG).[5] This model system was applied by Sommerfeld in the early days of quantum mechanics to study metals[6] and in 1965, Kohn and Sham[7] showed that the knowledge of a analytical parametrization of the UEG correlation energy allows one to perform approximate calculations for atoms, molecules, and solids. This spurred the development of a wide variety of spin-density correlation functionals (VWN,[8] PZ,[9] PW92,[10] etc.), each of which requires information on the high- and low-density regimes of the spin-polarized UEG, and are parametrized using numerical results from quantum Monte Carlo (QMC) calculations,[11,12] together with analytic perturbative results.

For this reason, a detailed and accurate understanding of the properties of the UEG ground state is essential to underpin the continued evolution of DFT. Moreover, meaningful comparisons between theoretical calculations on the UEG and realistic systems (such as sodium) have also been performed recently (see, e.g., Ref 13). The two-dimensional (2D) version of the UEG has also been the object of extensive research[14,15] because of its intimate connection to 2D or quasi-2D materials, such as quantum dots.[16,17] The one-dimensional (1D) UEG has recently attracted much attention due to its experimental realization in carbon nanotubes[18–22] organic conductors,[23–27] transition metal oxides,[28] edge states in quantum Hall liquids,[29–31] semiconductor heterostructures,[32–36] confined atomic gases,[37–39] and atomic or semiconducting nanowires.[40,41] In the present work, we have attempted to collect and collate the key results on the energetics of the UEG, information that is widely scattered throughout the physics and chemistry literature. The *UEG Paradigm* section defines and describes the UEG model in detail. The *High-Density Regime* section reports the known results for the high-density regime, wherein the UEG is a Fermi fluid (FF) of delocalized electrons. The *Low-Density Regime* section reports analogous results for the low-density regime, in

*Correspondence to: pf.loos@anu.edu.au

Research School of Chemistry, Australian National University, Canberra, Australia

Conflict of interest: The authors have declared no conflicts of interest for this article.

which the UEG becomes a Wigner crystal (WC) of relatively localized electrons. The intermediate-density results from QMC and symmetry-broken Hartree–Fock (SBHF) calculations are gathered in the *Intermediate-Density Regime* section. Atomic units are used throughout.

UEG PARADIGM

The D-dimensional UEG, or D-jellium, consists of interacting electrons in an infinite volume in the presence of a uniformly distributed background of positive charge. Traditionally, the system is constructed by allowing the number $n = n_\uparrow + n_\downarrow$ of electrons (where $n_\uparrow$ and $n_\downarrow$ are the numbers of spin-up and spin-down electrons, respectively) in a D-dimensional cube of volume V to approach infinity with the density $\rho = n/V$ held constant.[1] The spin polarization is defined as

$$\zeta = \frac{\rho_\uparrow - \rho_\downarrow}{\rho} = \frac{n_\uparrow - n_\downarrow}{n}, \tag{1}$$

where $\rho_\uparrow$ and $\rho_\downarrow$ is the density of the spin-up and spin-down electrons, respectively, and the $\zeta = 0$ and $\zeta = 1$ cases are called paramagnetic and ferromagnetic UEGs.

The total ground-state energy of the UEG (including the positive background) is

$$E[\rho] = T_\mathrm{s}[\rho] + \int \rho(\boldsymbol{r}) v(\boldsymbol{r}) d\boldsymbol{r} + J[\rho] + E_\mathrm{xc}[\rho] + E_\mathrm{b}, \tag{2}$$

where T_s is the noninteracting kinetic energy,

$$v(\boldsymbol{r}) = -\int \frac{\rho_\mathrm{b}(\boldsymbol{r}')}{|\boldsymbol{r}-\boldsymbol{r}'|} d\boldsymbol{r}' \tag{3}$$

is the external potential due to the positive background density ρ_b,

$$J[\rho] = \frac{1}{2}\int\int \frac{\rho(\mathbf{r})\rho(\mathbf{r}')}{|\mathbf{r}-\mathbf{r}'|} d\mathbf{r} d\mathbf{r}' \tag{4}$$

is the Hartree energy, E_xc is the exchange-correlation energy and

$$E_\mathrm{b} = \frac{1}{2}\int\int \frac{\rho_\mathrm{b}(\boldsymbol{r})\rho_\mathrm{b}(\boldsymbol{r}')}{|\boldsymbol{r}-\boldsymbol{r}'|} d\boldsymbol{r} d\boldsymbol{r}' \tag{5}$$

is the electrostatic self-energy of the positive background. The neutrality of the system [$\rho(\mathbf{r}) = \rho_\mathrm{b}(\mathbf{r})$] implies that

$$\int \rho(\boldsymbol{r}) v(\boldsymbol{r}) d\boldsymbol{r} + J[\rho] + E_\mathrm{b} = 0, \tag{6}$$

which yields

$$\begin{aligned} E[\rho] &= T_\mathrm{s}[\rho] + E_\mathrm{xc}[\rho] \\ &= T_\mathrm{s}[\rho] + E_\mathrm{x}[\rho] + E_\mathrm{c}[\rho] \\ &= \int \rho e_\mathrm{t}[\rho] d\boldsymbol{r} + \int \rho e_\mathrm{x}[\rho] d\boldsymbol{r} + \int \rho e_\mathrm{c}[\rho] d\boldsymbol{r}. \end{aligned} \tag{7}$$

In the following, we will focus on the three reduced (i.e., per electron) energies e_t, e_x, and e_c, and we will discuss these as functions of the Wigner–Seitz radius r_s defined via

$$\frac{1}{\rho} = \frac{\pi^{D/2}}{\Gamma\left(\frac{D}{2}+1\right)} r_s^D = \begin{cases} \frac{4\pi}{3} r_s^3, & D = 3, \\ \pi r_s^2, & D = 2, \\ 2 r_s, & D = 1, \end{cases} \tag{8}$$

or

$$r_s = \begin{cases} \left(\frac{3}{4\pi\rho}\right)^{1/3}, & D = 3, \\ \left(\frac{1}{\pi\rho}\right)^{1/2}, & D = 2, \\ \frac{1}{2\rho}, & D = 1, \end{cases} \tag{9}$$

where Γ is the Gamma function.[42] It is also convenient to introduce the Fermi wave vector

$$k_\mathrm{F} = \frac{\alpha}{r_s}, \tag{10}$$

where

$$\alpha = 2^{\frac{D-1}{D}} \Gamma\left(\frac{D}{2}+1\right)^{2/D} = \begin{cases} \left(\frac{9\pi}{4}\right)^{1/3}, & D = 3, \\ \sqrt{2}, & D = 2, \\ \frac{\pi}{4}, & D = 1. \end{cases} \tag{11}$$

THE HIGH-DENSITY REGIME

In the high-density regime ($r_s \ll 1$), also called the weakly correlated regime, the kinetic energy of the electrons dominates the potential energy, resulting in a completely delocalized system.[5] In this regime, the one-electron orbitals are plane waves and the UEG is described as a FF. Perturbation theory yields the energy expansion

$$e^{\mathrm{FF}}(r_s,\zeta) = e_{\mathrm{t}}(r_s,\zeta) + e_{\mathrm{x}}(r_s,\zeta) + e_{\mathrm{c}}^{\mathrm{FF}}(r_s,\zeta), \tag{12}$$

where the noninteracting kinetic energy $e_{\mathrm{t}}(r_s, \zeta)$ and exchange energy $e_{\mathrm{x}}(r_s, \zeta)$ are the zeroth- and first-order perturbation energies, respectively, and the correlation energy $e_{\mathrm{c}}^{\mathrm{FF}}(r_s,\zeta)$ encompasses all higher orders.

Noninteracting kinetic energy

The noninteracting kinetic energy of D-jellium is the first term of the high-density energy expansion (12). The 3D case has been known since the work of Thomas and Fermi[43,44] and, for D-jellium, it reads[45,46]

$$e_{\mathrm{t}}(r_s,\zeta) = \frac{\varepsilon_{\mathrm{t}}(\zeta)}{r_s^2}, \tag{13}$$

where

$$\varepsilon_{\mathrm{t}}(\zeta) = \varepsilon_{\mathrm{t}} Y_{\mathrm{t}}(\zeta), \tag{14a}$$

$$\varepsilon_{\mathrm{t}} \equiv \varepsilon_{\mathrm{t}}(\zeta = 0) = \frac{D}{2(D+2)}\alpha^2, \tag{14b}$$

and the spin-scaling function is

$$Y_{\mathrm{t}}(\zeta) = \frac{(1+\zeta)^{\frac{D+2}{D}} + (1-\zeta)^{\frac{D+2}{D}}}{2}. \tag{15}$$

The values of $\varepsilon_{\mathrm{t}}(\zeta)$ in the paramagnetic and ferromagnetic limits are given in Table 1 for D = 1, 2, and 3.

Exchange Energy

The exchange energy, which is the second term in (12), can be written[47,48]

$$e_{\mathrm{x}}(r_s,\zeta) = \frac{\varepsilon_{\mathrm{x}}(\zeta)}{r_s}, \tag{16}$$

where

$$\varepsilon_{\mathrm{x}}(\zeta) = \varepsilon_{\mathrm{x}} Y_{\mathrm{x}}(\zeta), \tag{17a}$$

$$\varepsilon_{\mathrm{x}} \equiv \varepsilon_{\mathrm{x}}(\zeta = 0) = -\frac{2D}{\pi(D^2-1)}\alpha, \tag{17b}$$

$$Y_{\mathrm{x}}(\zeta) = \frac{(1+\zeta)^{\frac{D+1}{D}} + (1-\zeta)^{\frac{D+1}{D}}}{2}. \tag{17c}$$

The values of $\varepsilon_{\mathrm{x}}(\zeta)$ in the paramagnetic and ferromagnetic limits are given in Table 1 for D = 1, 2, and

TABLE 1 | Energy Coefficients for the Paramagnetic (ζ = 0) and Ferromagnetic (ζ = 1) States and Spin-Scaling Functions of D-jellium at High Density

Term	Coefficient	Paramagnetic State $\varepsilon(0), \lambda(0)$			Ferromagnetic State $\varepsilon(1), \lambda(1)$			Spin-Scaling Function $Y(\zeta), \Lambda(\zeta)$		
		D = 1	D = 2	D = 3	D = 1	D = 2	D = 3	D = 1	D = 2	D = 3
r_s^{-2}	$\varepsilon_{\mathrm{t}}(\zeta)$	$\pi^2/96$	1/2	$\frac{3}{10}\left(\frac{9\pi}{4}\right)^{2/3}$	$\pi^2/24$	1	$2^{2/3}\frac{3}{10}\left(\frac{9\pi}{4}\right)^{2/3}$	1	Eq. (15)	Eq. (15)
r_s^{-1}	$\varepsilon_{\mathrm{x}}(\zeta)$	$-\infty$	$-\frac{4\sqrt{2}}{3\pi}$	$-\frac{3}{4\pi}\left(\frac{9\pi}{4}\right)^{1/3}$	$-\infty$	$-\frac{8}{3\pi}$	$-2^{1/3}\frac{3}{4\pi}\left(\frac{9\pi}{4}\right)^{1/3}$	1	Eq. (17c)	Eq. (17c)
ln r_s	$\lambda_0(\zeta)$	0	0	$\frac{1-\ln 2}{\pi^2}$	0	0	$\frac{1-\ln 2}{2\pi^2}$	—	—	Eq. (25)
r_s^0	$\varepsilon_0^a(\zeta)$	$-\pi^2/360$	ln 2 −1	−0.071 100	$-\pi^2/360$	$\frac{\ln 2 - 1}{2}$	−0.049 917	1	Eq. (44)	Ref 58
	$\varepsilon_0^b(\zeta)$	0	$\beta(2)-\frac{8}{\pi^2}\beta(4)$	$\frac{\ln 2}{6}-\frac{3}{4\pi^2}\zeta(3)$	0	$\beta(2)-\frac{8}{\pi^2}\beta(4)$	$\frac{\ln 2}{6}-\frac{3}{4\pi^2}\zeta(3)$	—	1	1
r_s ln r_s	$\lambda_1^a(\zeta)$	0	$-\sqrt{2}\left(\frac{10}{3\pi}-1\right)$	$\left(\frac{9\pi}{4}\right)^{1/3}\frac{\pi^2-6}{24\pi^3}$	0	$-\frac{1}{4}\left(\frac{10}{3\pi}-1\right)$	$\frac{1}{2^{1/3}}\left(\frac{9\pi}{4}\right)^{1/3}\frac{\pi^2+6}{24\pi^3}$	—	Eq. (39	Eq. (32a)
	$\lambda_1^b(\zeta)$	0	0	$\left(\frac{9\pi}{4}\right)^{1/3}\frac{\pi^2-12\ln 2}{4\pi^3}$	0	0	$\frac{1}{2^{4/3}}\left(\frac{9\pi}{4}\right)^{1/3}\frac{\pi^2-12\ln 2}{4\pi^3}$	—	—	Eq. (32b)
r_s	$e_1(\zeta)$	+ 0.008 446	unknown	−0.010	+ 0.008 446	unknown	unknown	1	unknown	unknown

Note that γ is the Euler-Mascheroni constant, $\zeta(n)$ is the Riemann zeta function and β is the Dirichlet β function.[42] In 1-jellium, the paramagnetic and ferromagnetic states are degenerate.

3. Note that, due to the particularly strong divergence of the Coulomb operator, $\varepsilon_x(\zeta)$ diverges in 1D.

Hartree–Fock Energy

In the high-density limit, one might expect the Hartree–Fock (HF) energy of the UEG to be the sum of the kinetic energy (13) and the exchange energy (16), i.e.,

$$e_{\mathrm{HF}}^{\mathrm{FF}}(r_s,\zeta) = e_t(r_s,\zeta) + e_x(r_s,\zeta). \tag{18}$$

However, although this energy corresponds to a solution of the HF equation, a stability analysis[5] reveals that (18) is never the lowest possible HF energy and Overhauser showed[49,50] that it is always possible to find a symmetry-broken solution of lower energy. We will discuss this further in the *Symmetry-broken Hartree-Fock* section.

In 1D systems, the Coulomb operator is so strongly divergent that a new term appears in the HF energy expression. Thus, for 1-jellium, Fogler found[51]

$$e_{\mathrm{HF}}^{\mathrm{FF}}(r_s) = \frac{\pi^2}{24r_s^2} - \frac{1}{2}\frac{\ln r_s}{r_s} + \frac{2\ln(\pi/2) - 3 + 2\gamma}{4r_s}, \tag{19}$$

where γ is the Euler–Mascheroni constant.[42] Furthermore, because the paramagnetic and ferromagnetic states are degenerate in strict 1D systems, we can confine our attention to the latter.[52–57]

Correlation Energy

The high-density correlation energy expansions

$$e_c^{\mathrm{FF}}(r_s,\zeta) = e(r_s,\zeta) - e_{\mathrm{HF}}^{\mathrm{FF}}(r_s,\zeta) \tag{20}$$

of the two- and three-dimensional UEGs have been well studied.[58–82] Much less is known about 1-jellium.[55,83] Using Rayleigh–Schrödinger perturbation theory, the correlation energy appears to possess the expansion

$$\begin{aligned} e_c^{\mathrm{FF}}(r_s,\zeta) &= \sum_{j=0}^{\infty} \left[\lambda_j(\zeta)\ln r_s + \varepsilon_j(\zeta)\right] r_s^j \\ &= \lambda_0(\zeta)\ln r_s + \varepsilon_0(\zeta) \\ &\quad + \lambda_1(\zeta) r_s \ln r_s + \varepsilon_1(\zeta) r_s + \ldots \end{aligned} \tag{21}$$

and the values of these coefficients (when known) are given in Table 1. The methods for their determination are outlined in the next three subsections.

3-jellium

The coefficient $\lambda_0(\zeta)$ can been obtained by the Gell-Mann–Brueckner resummation technique,[71] which sums the most divergent terms of the series (21) to obtain

$$\lambda_0(\zeta) = \frac{3}{32\pi^3}\int_{-\infty}^{\infty} [R_0(u,\zeta)]^2 du, \tag{22}$$

where

$$R_0(u,\zeta) = k_\downarrow R_0\left(\frac{u}{k_\downarrow}\right) + k_\uparrow R_0\left(\frac{u}{k_\uparrow}\right), \tag{23a}$$

$$R_0(u) = 1 - u\arctan(1/u), \tag{23b}$$

and

$$k_{\uparrow,\downarrow} = (1 \pm \zeta)^{1/D} \tag{24}$$

is the Fermi wave vector of the spin-up or spin-down electrons.

The paramagnetic[68] and ferromagnetic[74] limits are given in Table 1, and the spin-scaling function

$$\begin{aligned} \Lambda_0(\zeta) = \frac{1}{2} + \frac{1}{4(1-\ln 2)}\Big[& k_\downarrow k_\uparrow (k_\downarrow + k_\uparrow) - k_\downarrow^3 \\ & \ln\left(1 + \frac{k_\uparrow}{k_\downarrow}\right) - k_\uparrow^3 \ln\left(1 + \frac{k_\downarrow}{k_\uparrow}\right)\Big] \end{aligned} \tag{25}$$

was obtained by Wang and Perdew.[76]

The coefficient $\varepsilon_0(\zeta)$ is often written as the sum

$$\varepsilon_0(\zeta) = \varepsilon_0^{\mathrm{a}}(\zeta) + \varepsilon_0^{\mathrm{b}}(\zeta) \tag{26}$$

of a RPA (random-phase approximation) or 'ring-diagram' term $\varepsilon_0^{\mathrm{a}}(\zeta)$ and a first-order exchange term $\varepsilon_0^{\mathrm{b}}(\zeta)$. The RPA term $\varepsilon_0^{\mathrm{a}}(\zeta)$ is not known in closed form but it can be computed numerically with high precision.[58] Its paramagnetic and ferromagnetic limits are given in Table 1 and the spin-scaling function

$$\Upsilon_0^{\mathrm{a}}(\zeta) = \varepsilon_0^{\mathrm{a}}(\zeta)/\varepsilon_0^{\mathrm{a}}(0) \tag{27}$$

can be found using Eq. (20) in Ref 58. The first-order exchange term[75] is given in Table 1 and, because it is independent of the spin-polarization and the spin-scaling function

$$\Upsilon_0^{\mathrm{b}}(\zeta) = \varepsilon_0^{\mathrm{b}}(\zeta)/\varepsilon_0^{\mathrm{b}}(0) = 1 \tag{28}$$

is trivial.

The coefficient $\lambda_1(\zeta)$ can be written similarly[73] as

$$\lambda_1(\zeta) = \lambda_1^{\mathrm{a}}(\zeta) + \lambda_1^{\mathrm{b}}(\zeta), \tag{29}$$

where

$$\lambda_1^{\mathrm{a}}(\zeta) = -\frac{3\alpha}{8\pi^5}\int_{-\infty}^{\infty} \mathscr{R}_1^{\mathrm{a}}(u,\zeta)\,du, \tag{30a}$$

$$\lambda_1^{\mathrm{b}}(\zeta) = \frac{3\alpha}{16\pi^4}\int_{-\infty}^{\infty} \mathscr{R}_1^{\mathrm{b}}(u,\zeta)\,du \tag{30b}$$

are the RPA and second-order exchange contributions and α is given in (11). The integrands are[10,79]

$$\mathscr{R}_1^{\mathrm{a}}(u,\zeta) = R_0(u,\zeta)^2 R_1(u,\zeta), \tag{31a}$$

$$\mathscr{R}_1^{\mathrm{b}}(u,\zeta) = R_0(u,\zeta) R_2(iu,\zeta), \tag{31b}$$

$$R_1(u,\zeta) = k_\uparrow^{-1} R_1\left(\frac{u}{k_\uparrow}\right) + k_\downarrow^{-1} R_1\left(\frac{u}{k_\downarrow}\right), \tag{31c}$$

$$R_2(iu,\zeta) = R_2\left(i\frac{u}{k_\uparrow}\right) + R_2\left(i\frac{u}{k_\downarrow}\right), \tag{31d}$$

$$R_1(u) = -\frac{\pi}{3(1+u^2)^2}, \tag{31e}$$

$$R_2(iu) = 4\frac{(1+3u^2) - u(2+3u^2)\arctan u}{1+u^2}. \tag{31f}$$

Carr and Maradudin gave an estimate[73] of $\lambda_1(0)$ and this was later refined by Perdew et al.[10,79]

However, we have found[80] that the integrals in Eqs. (30a) and (30b) can be evaluated exactly by computer software,[84] giving the paramagnetic and ferromagnetic values in Table 1 and the spin-scaling functions

$$\begin{aligned}\Lambda_1^{\mathrm{a}}(\zeta) &= \frac{3}{\pi^2-6}\left\{\left(\frac{\pi^2}{6}+\frac{1}{4}\right)\left(k_\uparrow^2+k_\downarrow^2\right)\right.\\ &\quad -\frac{3}{2}k_\uparrow k_\downarrow - \frac{k_\uparrow^2+k_\downarrow^2}{k_\uparrow^2-k_\downarrow^2}k_\uparrow k_\downarrow \ln\left(\frac{k_\uparrow}{k_\downarrow}\right)\\ &\quad \left.-\frac{k_\uparrow^2-k_\downarrow^2}{2}\left[\mathrm{Li}_2\left(\frac{k_\uparrow-k_\downarrow}{k_\uparrow+k_\downarrow}\right)-\mathrm{Li}_2\left(\frac{k_\downarrow-k_\uparrow}{k_\uparrow+k_\downarrow}\right)\right]\right\},\end{aligned} \tag{32a}$$

$$\begin{aligned}\Lambda_1^{\mathrm{b}}(\zeta) &= \frac{3}{\pi^2-12\ln 2}\left\{\frac{\pi^2}{6}\left(k_\uparrow^2+k_\downarrow^2\right)\right.\\ &\quad +(1-\ln 2)\left(k_\uparrow-k_\downarrow\right)^2 - \frac{k_\uparrow^2}{2}\mathrm{Li}_2\left(\frac{k_\uparrow-k_\downarrow}{k_\uparrow+k_\downarrow}\right)\\ &\quad -\frac{k_\downarrow^2}{2}\mathrm{Li}_2\left(\frac{k_\downarrow-k_\uparrow}{k_\uparrow+k_\downarrow}\right)+\frac{1}{k_\uparrow k_\downarrow}\left[k_\uparrow^4\ln\left(\frac{k_\uparrow}{k_\uparrow+k_\downarrow}\right)\right.\\ &\quad \left.\left.+k_\uparrow^2k_\downarrow^2\ln\left(\frac{k_\uparrow k_\downarrow}{(k_\uparrow+k_\downarrow)^2}\right)+k_\downarrow^4\ln\left(\frac{k_\downarrow}{k_\uparrow+k_\downarrow}\right)\right]\right\},\end{aligned} \tag{32b}$$

where Li_2 is the dilogarithm function.[42]

The spin scalings $\Lambda_0(\zeta)$, $\Upsilon_0^{\mathrm{a}}(\zeta)$, $\Upsilon_0^{\mathrm{b}}(\zeta)$, $\Lambda_1^{\mathrm{a}}(\zeta)$, and $\Lambda_1^{\mathrm{b}}(\zeta)$ are shown in Figure 1, highlighting the Hoffmann minimum[58] in $\Upsilon_0^{\mathrm{a}}(\zeta)$ near $\zeta = 0.9956$ and revealing a similar minimum in $\Lambda_1^{\mathrm{a}}(\zeta)$ near $\zeta = 0.9960$. It appears that such minima are ubiquitous in RPA coefficients.

The data in Table 1 yield the exact values

$$\begin{aligned}\lambda_1(0) &= \frac{\alpha}{4\pi^3}\left(\frac{7\pi^2}{6}-12\ln 2-1\right)\\ &= 0.009229\ldots,\end{aligned} \tag{33a}$$

$$\begin{aligned}\lambda_1(1) &= 2^{-4/3}\frac{\alpha}{4\pi^3}\left(\frac{13\pi^2}{12}-12\ln 2+\frac{1}{2}\right)\\ &= 0.004792\ldots,\end{aligned} \tag{33b}$$

and it is revealing to compare these with recent numerical calculations. The estimate $\lambda_1(0) \approx 0.0092292$ by Sun et al.[79] agrees perfectly with Eq. (33a) but their estimate $\lambda_1(1) \approx 0.003125$ is strikingly different from Eq. (33b). The error arises from the noncommutivity of the $\zeta \to 1$ limit and the u integration, which is due to the nonuniform convergence of $\mathscr{R}_1^{\mathrm{a}}(u,\zeta)$.

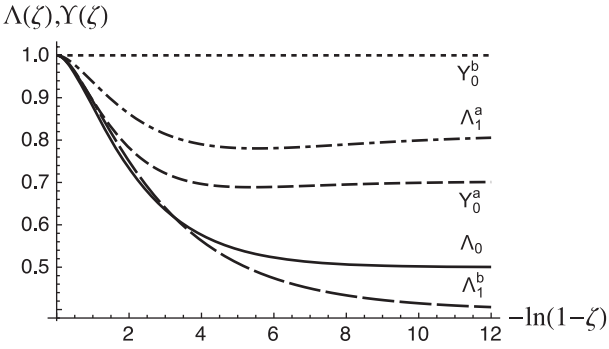

FIGURE 1 | Spin-scaling functions of 3-jellium as functions of ζ.

Based on the work of Carr and Maradundin,[73] Endo et al.[77] have been able to obtain a numerical value

$$\varepsilon_1(0) = -0.010 \tag{34}$$

for the paramagnetic limit of the term proportional to r_s. However, nothing is known about the spin-scaling function and the ferromagnetic value for this coefficient. Calculations by one of the present authors suggest that the value (34) is probably not accurate,[85] mainly due to the large errors in the numerical integrations performed in Ref 73.

2-jellium

Gell-Mann–Brueckner resummation for 2-jellium yields[61]

$$\lambda_0(\zeta) = 0, \tag{35a}$$

$$\lambda_1(\zeta) = -\frac{1}{12\sqrt{2}\pi}\int_{-\infty}^{\infty}\left[R\left(\frac{u}{k_\uparrow}\right) + R\left(\frac{u}{k_\downarrow}\right)\right]^3 du, \tag{35b}$$

where

$$R(u) = 1 - \frac{1}{\sqrt{1+1/u^2}}. \tag{36}$$

After an unsuccessful attempt by Zia,[59] the correct values of the coefficients $\lambda_1(0)$ and $\lambda_1(1)$ were found by Rajagopal and Kimball[61] to be

$$\lambda_1(0) = -\sqrt{2}\left(\frac{10}{3\pi} - 1\right) = -0.086314\ldots, \tag{37}$$

and[74]

$$\lambda_1(1) = \frac{\sqrt{2}}{8}\lambda_1(0) = -\frac{1}{4}\left(\frac{10}{3\pi} - 1\right) = -0.015258\ldots. \tag{38}$$

Thirty years later, Chesi and Giuliani found[66] the spin-scaling function

$$\Lambda_1(\zeta) = \frac{\lambda_1(\zeta)}{\lambda_1(0)} = \frac{1}{8}\left[k_\uparrow + k_\downarrow + 3\frac{F(k_\uparrow,k_\downarrow) + F(k_\downarrow,k_\uparrow)}{10-3\pi}\right] \tag{39}$$

where

$$F(x,y) = 4(x+y) - \pi x - 4xE\left(1 - \frac{y^2}{x^2}\right) + 2x^2\frac{\arccos\frac{y}{x}}{\sqrt{x^2-y^2}}, \tag{40}$$

and $E(x)$ is the complete elliptic integral of the second kind.[42]

As in 3-jellium, the constant term $\varepsilon_0(\zeta)$ can be decomposed into a direct contribution $\varepsilon_0^{\mathrm{a}}(\zeta)$ and a ζ-independent exchange contribution $\varepsilon_0^{\mathrm{b}}$

$$\varepsilon_0(\zeta) = \varepsilon_0^{\mathrm{a}}(\zeta) + \varepsilon_0^{\mathrm{b}}. \tag{41}$$

Following Onsager's work on the 3D case,[75] Isihara and Ioriatti showed[63] that

$$\varepsilon_0^{\mathrm{b}} = \beta(2) - \frac{8}{\pi^2}\beta(4) = +0.114357\ldots, \tag{42}$$

where $G = \beta(2)$ is the Catalan's constant and β is the Dirichlet β function.[42] Recently, we have found closed-form expressions for the direct part $\varepsilon_0^{\mathrm{a}}(\zeta)$.[67] The paramagnetic and ferromagnetic limits are

$$\varepsilon_0^{\mathrm{a}}(0) = \ln 2 - 1 = -0.306853\ldots, \tag{43a}$$

$$\varepsilon_0^{\mathrm{a}}(1) = \frac{1}{2}\varepsilon_0^{\mathrm{a}}(0) = \frac{\ln 2 - 1}{2} = -0.153426\ldots, \tag{43b}$$

and the spin-scaling functions are

$$\begin{aligned}\Upsilon_0^{\mathrm{a}}(\zeta) &= \frac{1}{2} + \frac{1-\zeta}{4(\ln 2 - 1)}\left[2\ln 2 - 1\right. \\ &\quad - \sqrt{\frac{1+\zeta}{1-\zeta}} + \frac{1+\zeta}{1-\zeta}\ln\left(1 + \sqrt{\frac{1-\zeta}{1+\zeta}}\right) \\ &\quad \left. - \ln\left(1 + \sqrt{\frac{1+\zeta}{1-\zeta}}\right)\right].\end{aligned} \tag{44}$$

and $\Upsilon_0^{\mathrm{b}}(\zeta) = 1$. The spin-scaling functions of 2-jellium are plotted in Figure 2. To the best of our knowledge, the term proportional to r_s in the high-density expansion of the correlation energy (21) is unknown for 2-jellium.

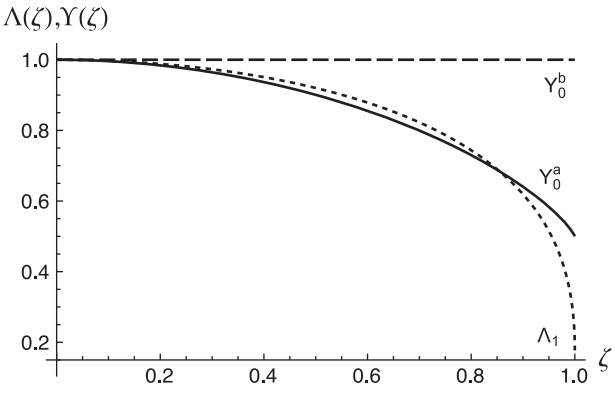

FIGURE 2 | Spin-scaling functions of 2-jellium as functions of ζ.

1-jellium

Again, due to the strong divergence of the Coulomb operator in 1D, 1-jellium is peculiar and one has to take special care.[57] More details can be found in Ref 83. The leading term of the high-density correlation energy in 1-jellium has been found to be[83]

$$\varepsilon_0 = -\frac{\pi^2}{360} = -0.027416\ldots, \tag{45}$$

and third-order perturbation theory gives[73,83]

$$\varepsilon_1 = +0.008446. \tag{46}$$

We note that 1-jellium is one of the few systems where the r_s coefficient of the high-density expansion is known accurately.[77,79] Unlike 2- and 3-jellium, the expansion (21) does not contain any logarithm term up to first order in r_s, i.e., $\lambda_0 = \lambda_1 = 0$. The high-density expansion of the correlation of 1-jellium is

$$e_c^{\mathrm{FF}}(r_s) = -\frac{\pi^2}{360} + 0.008446 r_s + \ldots. \tag{47}$$

THE LOW-DENSITY REGIME

In the low-density (or strongly correlated) regime, the potential energy dominates over the kinetic energy and the electrons localize onto lattice points that minimize their (classical) Coulomb repulsion.[86,87] These minimum-energy configurations are called Wigner crystals.[88] In this regime, strong-coupling methods[89] can be used to show that the WC energy has the asymptotic expansion

$$e^{\mathrm{WC}}(r_s) \sim \sum_{j=0}^{\infty} \frac{\eta_j}{r_s^{j/2+1}} = \frac{\eta_0}{r_s} + \frac{\eta_1}{r_s^{3/2}} + \frac{\eta_2}{r_s^2} + \frac{\eta_3}{r_s^{5/2}} + \ldots. \tag{48}$$

This equation is usually assumed to be strictly independent of the spin polarization.[5,10,79,90] The values of the low-density coefficients for D-jellium are reported in Table 2

TABLE 2 | Energy Coefficients of D-jellium at Low Density

Term	Coeff.	$D = 3$ bcc Lattice	$D = 2$ Δ Lattice	$D = 1$ Linear Lattice
r_s^{-1}	η_0	− 0.895 930	− 1.106 103	$(\gamma - \ln 2)/2$
$r_s^{-3/2}$	η_1	1.325	0.795	0.359933
r_s^{-2}	η_2	− 0.365	unknown	unknown

Note that γ is the Euler-Mascheroni constant.[42]

3-jellium

The leading term of the low-density expansion η_0 is the Madelung constant for the WC.[91] In 3D, Coldwell-Horsfall and Maradudin have studied several lattices: simple cubic (sc), face-centered cubic (fcc), and body-centered cubic (bcc). Carr also mentions[92] a calculation for the hexagonal closed pack (hcp) by Kohn and Schechter.[93] The values of η_0 for these lattices are

$$\eta_0^{\mathrm{sc}} = -0.880059\ldots, \tag{49a}$$

$$\eta_0^{\mathrm{hcp}} = -0.895838\ldots, \tag{49b}$$

$$\eta_0^{\mathrm{fcc}} = -0.895877\ldots, \tag{49c}$$

$$\eta_0^{\mathrm{bcc}} = -0.895930\ldots. \tag{49d}$$

and reveal that, although all four lattices are energetically similar, the bcc lattice is the most stable.

For the bcc WC, Carr subsequently derived[92] the harmonic zero-point energy coefficient

$$\eta_1 = 1.325, \tag{50}$$

and the first anharmonic coefficient[94]

$$\eta_2 = -0.365. \tag{51}$$

Based on an interpolation, Carr et al.[94] estimated the next term of the low-density asymptotic expansion to be $\eta_3 \approx -0.4$.

Combining Eqs. (49d), (50), and (51) yields the low-density energy expansion of the 3D bcc WC

$$e^{\mathrm{WC}}(r_s) \sim -\frac{0.895930}{r_s} + \frac{1.325}{r_s^{3/2}} - \frac{0.365}{r_s^2} + \ldots. \tag{52}$$

2-jellium

Following the same procedure as for 3-jellium, Bonsall and Maradudin[95] derived the leading term of the low-density energy expansion of the 2D WC for the square (□) and triangular (Δ) lattices:

$$\eta_0^{\square} = -\frac{1}{\sqrt{\pi}}\left\{2 - \sum_{\ell_1,\ell_2}{}' E_{-1/2}\left[\pi\left(\ell_1^2 + \ell_2^2\right)\right]\right\} = -1.100244\ldots, \tag{53a}$$

$$\eta_0^{\Delta} = -\frac{1}{\sqrt{\pi}}\left\{2 - \sum_{\ell_1,\ell_2}{}' E_{-1/2}\left[\frac{2\pi}{\sqrt{3}}\left(\ell_1^2 - \ell_1\ell_2 + \ell_2^2\right)\right]\right\} = -1.106103\ldots, \tag{53b}$$

where

$$E_{-1/2}(x) = \frac{1}{x}\left(\frac{\sqrt{\pi}}{2}\frac{\mathrm{erfc}(\sqrt{x})}{\sqrt{x}} + e^{-x}\right), \qquad (54)$$

erfc is the complementary error function[42] and the prime excludes $(\ell_1, \ell_2) = (0, 0)$ from the summation. This shows that the triangular (hexagonal) lattice is more stable than the square one.

For the triangular lattice, Bonsall and Maradundin[95] also derived the harmonic coefficient

$$\eta_1 = 0.795, \qquad (55)$$

but, to our knowledge, the first anharmonic coefficient is unknown. This yields the 2D WC energy expression

$$e^{\mathrm{WC}}(r_s) \sim -\frac{1.106103}{r_s} + \frac{0.795}{r_s^{3/2}} + \ldots. \qquad (56)$$

1-jellium

The first two coefficients of the low-density energy expansion of 1-jellium can be found in Fogler's work.[51] The present authors have also given an alternative, simpler derivation using uniformly spaced electrons on a ring.[55,96] Both constructions lead to

$$\eta_0 = \frac{\gamma - \ln 2}{2} = -0.057966\ldots, \qquad (57a)$$

$$\eta_1 = \frac{1}{4\pi}\int_0^{\pi}\sqrt{2\mathrm{Li}_3(1) - \mathrm{Li}_3(e^{i\theta}) - \mathrm{Li}_3(e^{-i\theta})}\,d\theta = +0.359933\ldots. \qquad (57b)$$

where Li_3 is the trilogarithm function[42] and the energy expansion is

$$e^{\mathrm{WC}}(r_s) \sim \frac{\gamma - \ln 2}{2r_s} + \frac{0.359933}{r_s^{3/2}} + \ldots. \qquad (58)$$

THE INTERMEDIATE-DENSITY REGIME

Quantum Monte Carlo

Although it is possible to obtain information on the high- and low-density limits using perturbation theory, this approach struggles in the intermediate-density regime because of the lack of a suitable reference. As a result, quantum Monte Carlo (QMC) techniques[97,98] and, in particular, diffusion Monte Carlo (DMC) calculations have been valuable in this density range. The first QMC calculations on 2- and 3-jellium were reported in 1978 by Ceperley.[11] Although QMC calculations have limitations (finite-size effect,[99–103] fixed-node error,[104–117] etc), these paved the way for much subsequent research on the UEG and, indirectly, on the development of DFT.[1]

3-jellium

Two years after Ceperley's seminal paper,[11] Ceperley and Alder published QMC results[12] that were subsequently used by various authors[8–10] to construct UEG correlation functionals. In their paper, Ceperley and Alder published released-node DMC results for the paramagnetic and ferromagnetic FF as well as the Bose fluid and bcc crystal. Using these data, they proposed the first complete phase diagram of 3-jellium and, despite its being based on a Bose bcc crystal, it is more than qualitatively correct, as we will show later. In particular, they found that 3-jellium has two phase transitions: a polarization transition (from paramagnetic to ferromagnetic fluid) at $r_s = 75 \pm 5$ and a ferromagnetic fluid-to-crystal transition at $r_s = 100 \pm 20$.

In the 1990's, Ortiz et al. extended Ceperley's study to partially polarized fluid.[118–120] They discovered a continuous transition from the paramagnetic to the ferromagnetic state in the range $20 \pm 5 \le r_s \le 40 \pm 5$ and they also predicted a much lower crystallization density ($r_s = 65 \pm 10$) than Ceperley and Alder.

Using more accurate trial wave function (with backflow)[121] and twist-averaged boundary conditions[100] (to minimize finite-size effects), Zong et al.[122] re-evaluated the energy of the paramagnetic, ferromagnetic, and partially polarized fluid at relatively low density ($40 \le r_s \le 100$). They found a second-order transition to a ferromagnetic phase at $r_s = 50 \pm 2$. According to their results, the ferromagnetic fluid becomes more stable than the paramagnetic one at $r_s \approx 80$.

To complete the picture, Drummond et al.[123] reported an exhaustive and meticulous study of the 3D WC over the range $100 \le r_s \le 150$. They concluded that 3-jellium undergoes a transition from a ferromagnetic fluid to a bcc WC at $r_s = 106 \pm 1$, confirming the early prediction of Ceperley and Alder.[12] The discrepancy between the crystallization density found by Ortiz et al.[120] and the one determined by Drummond et al.[123] is unclear.[a] The latter authors have also investigated the possibility of the existence of an antiferromagnetic WC phase but, sadly, they concluded that the energy difference

between the ferromagnetic and antiferromagnetic crystals was too small to resolve in their DMC calculations. More recently, Spink et al.[124] have also reported very accurate DMC energies for the partially polarized fluid phase at moderate density ($0.2 \le r_s \le 20$).

The DMC energies of 3-jellium (for the FF and WC phases) have been gathered in Table 4 for various r_s and ζ values. Combining the DMC results of Zong et al.[122] and Drummond et al.,[123] we have represented the phase diagram of 3-jellium in Figure 3. The correlation energy of the paramagnetic and ferromagnetic fluids is fitted using the parametrization proposed by Ceperley[11]

$$e_c^{\mathrm{FF}}(r_s) = \frac{a_0}{1 + a_1\sqrt{r_s} + a_2 r_s}, \tag{59}$$

where a_0, a_1, and a_2 are fitting parameters. For the ferromagnetic fluid, we have used the values of a_0, a_1, and a_2 given in Ref 123. These values have been obtained by fitting the ferromagnetic results of Zong et al.[122] For the paramagnetic state, we have fitted the paramagnetic results of Ref 122, and found the values given in Table 3.

To parametrize the WC energy data, Drummond et al.[123] used another expression proposed by Ceperley[11]

$$e^{\mathrm{WC}}(r_s) = \frac{b_0}{r_s} + \frac{b_1}{r_s^{3/2}} + \frac{b_2}{r_s^2}. \tag{60}$$

The first coefficient b_0 is taken to be equal to the low-density limit expansion η_0 (see *The Low-Density Regime* section), while b_1 and b_2 are obtained by fitting the DMC results of Ref 123.

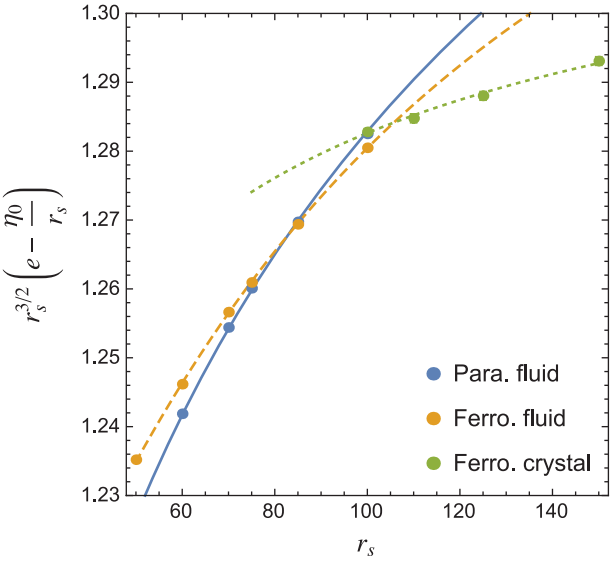

FIGURE 3 | Diffusion Monte Carlo phase diagram of 3-jellium.

TABLE 3 | Values of the Coefficients a_0, a_1, and a_2 in Eq. (59) and b_0, b_1, and b_2 in Eq. (60) Used to Parametrize the Energy of 3-jellium in the FF and WC Phases

Fermi Fluid			Wigner Crystal	
Coefficient	Para.	Ferro.	Coefficient	Ferro.
a_0	−0.214488	−0.09399	b_0	−0.89593
a_1	1.68634	1.5268	b_1	1.3379
a_2	0.490538	0.28882	b_2	−0.55270

FF, Fermi fluid; WC, Wigner crystal.

2-jellium

The first exhaustive study of 2-jellium at the DMC level was published in 1989 by Tanatar and Ceperley.[125] In their study, the authors investigate the paramagnetic and ferromagnetic fluid phases, as well as the ferromagnetic WC with hexagonal symmetry (triangular lattice). They discovered a Wigner crystallization at $r_s = 37 \pm 5$ and they found that, although they are very close in energy, the paramagnetic fluid is always more stable than the ferromagnetic one. Although the Tanatar–Ceperley energies are systematically too low, as noted by Kwon et al.,[126] their phase diagram is qualitatively correct.

A few years later, Rapisarda and Senatore[127] revisited the phase diagram of 2-jellium. They found a region of stability for the ferromagnetic fluid with a polarization transition at $r_s = 20 \pm 2$ and observed a ferromagnetic fluid-to-crystal transition at $r_s = 34 \pm 4$. This putative region of stability for the ferromagnetic fluid was also observed by Attaccalite et al.[128–130] who obtained a similar phase diagram with a polarization transition at $r_s \approx 26$ and a crystallization at $r_s \approx 35$. An important contribution of Ref 128 was to show that, in contrast to 3-jellium, the partially polarized FF is never a stable phase of 2-jellium.

More recently, and in contrast to earlier QMC studies, Drummond and Needs[131] obtained statistical errors sufficiently small to resolve the energy difference between the ferromagnetic and paramagnetic fluids. Interestingly, instead of observing a transition from the ferromagnetic fluid to the ferromagnetic crystal, they discovered a transition from the paramagnetic fluid to an antiferromagnetic crystal around $r_s = 31 \pm 1$. Moreover, they also showed that the ferromagnetic fluid is never more stable than the paramagnetic one, and that it is unlikely that a region of stability exists for a partially spin-polarized fluid. This agrees with the earlier work of Attaccalite et al.[128] However, they did find a transition from the

antiferromagnetic to the ferromagnetic WC at $r_s = 38 \pm 5$.

Some authors have investigated the possibility of the existence of a 'hybrid phase' in the vicinity of the transition density from ferromagnetic fluid to ferromagnetic WC.[131–135] According to Falakshahi and Waintal,[133,134] the hybrid phase has the same symmetry as the WC but has partially delocalized orbitals. However, its existence is still under debate.[131]

The DMC energies of 2-jellium (for the fluid and crystal phases) have been gathered in Table 4 for various r_s. Based on the data of Ref 131, we have constructed the phase diagram of 2-jellium in Figure 4. The fluid energy data are fitted using the parametrization proposed by Rapisarda and Senatore:[127]

$$e_c^{FF}(r_s) = a_0\left\{1 + Ar_s\left[B\ln\frac{\sqrt{r_s}+a_1}{\sqrt{r_s}} + \frac{C}{2}\ln\frac{r_s+2a_2\sqrt{r_s}+a_3}{r_s} + D\left(\arctan\frac{\sqrt{r_s}+a_2}{\sqrt{a_3-a_2^2}} - \frac{\pi}{2}\right)\right]\right\}, \quad (61)$$

where

$$A = \frac{2(a_1+2a_2)}{2a_1a_2-a_3-a_1^2}, \quad B = \frac{1}{a_1} - \frac{1}{a_1+2a_2}, \quad (62a)$$

$$C = \frac{a_1}{a_3} - \frac{2a_2}{a_3} + \frac{1}{a_1+2a_2}, \quad D = \frac{F-a_2C}{\sqrt{a_3-a_2^2}}, \quad (62b)$$

$$F = 1 + (2a_2-a_1)\left(\frac{1}{a_1+2a_2} - \frac{2a_2}{a_3}\right). \quad (62c)$$

To parametrize the WC energies, Drummond and Needs[131] used the expression proposed by Ceperley[11]

$$e^{WC}(r_s) = \frac{b_0}{r_s} + \frac{b_1}{r_s^{3/2}} + \frac{b_2}{r_s^2} + \frac{b_3}{r_s^{5/2}} + \frac{b_4}{r_s^3}. \quad (63)$$

The first two coefficients b_0 and b_1 are taken to be equal to the low-density limit expansion η_0 and η_1 (see *The Low-Density Regime* section), and the others are found by fitting to their DMC results. The values of the fitting coefficients for 2-jellium are given in Table 5.

1-jellium

Not surprisingly, there have been only a few QMC studies on 1-jellium. Astrakharchik and Girardeau[52] have studied 1-jellium qualitatively from the high to the low-density regimes. Lee and Drummond[53] have published accurate DMC data for the range $1 \le r_s \le 20$. The present authors have published DMC data at higher and lower densities in order to parametrize a generalized version of the LDA.[55,56,96] The DMC data for 1-jellium are reported in Table 6.

Using the 'robust' interpolation proposed by Cioslowski[136] and the high- and low-density expansions (47) and (58), the correlation energy of 1-jellium calculated with the HF energy given by (19) can be approximated by

$$e_c^{LDA}(r_s) = t^2\sum_{j=0}^{3} c_j t^j (1-t)^{3-j}, \quad (64)$$

with

$$t = \frac{\sqrt{1+4kr_s}-1}{2kr_s}, \quad (65)$$

and

$$c_0 = k\eta_0, \quad c_1 = 4k\eta_0 + k^{3/2}\eta_1, \quad (66a)$$

$$c_2 = 5\varepsilon_0 + \varepsilon_1/k, \quad c_3 = \varepsilon_1, \quad (66b)$$

where $k = 0.414254$ is a scaling factor which is determined by a least-squares fit of the DMC data given in Refs 53 and 55.

The results using the LDA correlation functional (64) are compared to the DMC calculations of Refs 53 and 55. The results are gathered in Table 7 and depicted in Figure 5. For $0.2 \le r_s \le 100$, the LDA and DMC correlation energies agree to within 0.1 millihartree, which is remarkable given the simplicity of the functional.

Symmetry-broken Hartree-Fock

In the early 1960s, Overhauser[49,50] showed that the HF energy (18) for the paramagnetic FF can always be improved by following spin- and charge-density instabilities[5] to locate a SBHF solution. Recently, a computational 'proof' has been given by Zhang and Ceperley[137] who performed unrestricted HF (UHF) calculations on the paramagnetic state of finite-size 3D UEGs and discovered broken spin-symmetry solutions, even for high densities. In 2D, this has been proven rigorously for the ferromagnetic state by Bernu et al.[138] The first phase diagrams based on UHF calculations for 2- and 3-jellium were performed by Trail et al.[139] who found lower energies

TABLE 4 | DMC Energy of 3-jellium at Various r_s for the FF and WC Phases

r_s	Para. Fluid	Partially Spin-Polarized Fluid					Ferro. Fluid	Ferro. Crystal
	$\zeta = 0$	$\zeta = 0.185$	$\zeta = 0.333$	$\zeta = 0.519$	$\zeta = 0.667$	$\zeta = 0.852$	$\zeta = 1$	$\zeta = 1$
0.5	3.430 11(4)	—	3.692 87(6)	—	4.441 64(6)	—	5.824 98(2)	—
1	0.587 80(1)	—	0.649 19(2)	—	0.823 94(4)	—	1.146 34(2)	—
2	0.002 380(5)	—	0.016 027(6)	—	0.054 75(2)	—	0.126 29(3)	—
3	−0.067 075(4)	—	−0.061 604(5)	—	−0.046 08(2)	—	−0.017 278(4)	—
5	−0.075 881(1)	—	−0.074 208(4)	—	−0.069 548(4)	—	−0.060 717(5)	—
10	−0.053 511 6(5)	—	−0.053 214(2)	—	−0.052 375(2)	—	−0.050 733 7(5)	—
20	−0.031 768 6(5)	—	−0.031 715 6(7)	—	−0.031 594 0(7)	—	−0.031 316 0(4)	—
40	−0.017 618 7(3)	—	−0.017 6165(3)	—	−0.017 602 7(3)	—	−0.017 567 4(4)	—
50	−0.014 449 5(3)	−0.014 449 5(3)	−0.014 449 8(3)	−0.014 447 3(4)	−0.014 444 2(3)	−0.014 437 7(4)	−0.014 424 9(4)	—
60	−0.012 260 1(2)	−0.012 259 3(3)	−0.012 260 2(2)	−0.012 259 8(3)	−0.012 258 7(2)	−0.012 255 9(2)	−0.012 250 8(2)	—
70	−0.010 657 2(2)	−0.010 656 9(2)	−0.010 658 1(2)	−0.010 658 6(3)	−0.010 658 0(2)	−0.010 656 7(2)	−0.010 653 3(2)	—
75	−0.010 005 7(2)	−0.010 006 0(2)	−0.010 006 9(2)	—	−0.010 007 2(2)	—	−0.010 004 4(2)	—
85	−0.008 920 1(2)	—	−0.008 9208(2)	—	−0.008 921 5(2)	—	−0.008 920 6(2)	—
100	−0.007 676 8(2)	—	−0.007 677(2)	—	−0.007 678 2(1)	—	−0.007 678 8(1)	−0.007 676 5(4)
110	—	—	—	—	—	—	—	−0.007 031 2(5)
125	—	—	—	—	—	—	—	−0.006 245 8(4)
150	—	—	—	—	—	—	—	−0.005 269 0(3)

For the FF, the data from r_s = 0.5 to 20 are taken from Ref 124, and the data from r_s = 40 to 100 are taken from Ref 122. The data for the ferromagnetic WC are taken from Ref 123. The statistical error is reported in parenthesis.
DMC, Diffusion Monte Carlo; FF, Fermi fluid; WC, Wigner crystal.

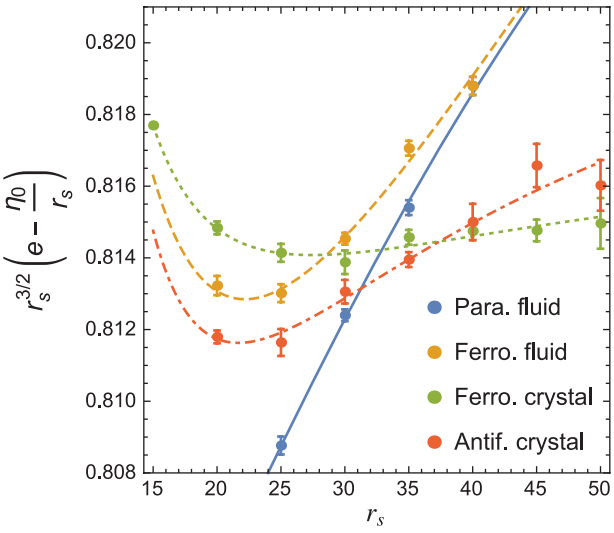

FIGURE 4 | Diffusion Monte Carlo phase diagram of 2-jellium.

for a crystal for $r_s > 1.44$ in 2D and $r_s > 4.5$ in 3D. Curiously, as we will show below, the SBHF phase diagram is far richer than the near-exact DMC one presented in the *Quantum Monte Carlo* section.

Before going further, it is interesting to investigate the HF expression of the FF given by (18), and study the phase diagram based on this simple expression[5] (see Figure 6 for the example of 3-jellium). It is easy to show that, for $0 < r_s < r_s^{\mathrm{B}}$, the paramagnetic fluid is predicted to be lower in energy than the ferromagnetic fluid where

$$r_s^{\mathrm{B}} = -\frac{2^{2/D}-1}{2^{1/D}-1}\frac{\varepsilon_t}{\varepsilon_x} = \begin{cases} 2.011, & D=2, \\ 5.450, & D=3, \end{cases} \tag{67}$$

and ε_t and ε_x are given by Eqs. (14b) and (17b), respectively. This sudden paramagnetic-to-

TABLE 5 | Values of the Coefficients a_0, a_1, a_2, and a_3 in Eq. (61) and b_0, b_1, b_2 and b_3 and b_4 in Eq. (63) Used to Parameterize the Energy of 2-jellium in the FF and WC Phases

Fermi Fluid			Wigner Crystal		
	Value			Value	
Coefficient	Para. Fluid	Ferro. Fluid	Coefficient	Ferro. Crystal	Antif. Crystal
a_0	−0.186 305 2	−0.290 910 2	b_0	−1.106 103	−1.106 103
a_1	6.821 839	−0.624 383 6	b_1	0.814	0.814
a_2	0.155 226	1.656 628	b_2	0.113 743	0.266 297 7
a_3	3.423 013	3.791 685	b_3	−1.184 994	−2.632 86
			b_4	3.097 610	6.246 358

FF, Fermi fluid; WC, Wigner crystal.

TABLE 6 | DMC Energy of 2-jellium at Various r_s for the FF and WC Phases

r_s	Para. Fluid $\zeta = 0$	Ferro. Fluid $\zeta = 1$	Antif. Crystal $\zeta = 0$	Ferro. Crystal $\zeta = 1$
1	− 0.209 8(3)	—	—	—
5	− 0.149 5(1)	− 0.143 3(1)	—	—
10	− 0.085 36(2)	− 0.084 48(4)	—	—
15	—	—	—	− 0.059 665(1)
20	− 0.046 305(4)	− 0.046 213(3)	− 0.046 229(2)	− 0.046 195(2)
25	− 0.037 774(2)	− 0.037 740(2)	− 0.037 751(3)	− 0.037 731(2)
30	− 0.031 926(1)	− 0.031 913(1)	− 0.031 922(2)	− 0.031 917(2)
35	− 0.027 665(1)	− 0.027 657(1)	− 0.027 672(1)	− 0.027 669(1)
40	− 0.024 416(1)	− 0.024 416(1)	− 0.024 431(2)	− 0.024 432(1)
45	—	—	− 0.021 875(2)	− 0.021 881(1)
50	—	—	− 0.019 814(2)	− 0.019 817(2)

Data from r_s = 1 to 10 are taken from Ref 126 for the paramagnetic fluid. Data from r_s = 5 to 10 are taken from Ref 127 for the ferromagnetic fluid. Data from r_s = 15 to 50 are taken from Ref 131. The statistical error is reported in parenthesis.
DMC, diffusion Monte Carlo; FF, Fermi fluid; WC, Wigner crystal.

TABLE 7 | DMC Energy and Reduced Energy Given by Eq. (66a) for 1-jellium at Various r_s

r_s	DMC Energy	$e_{HF}^{FF}+e_c^{LDA}$
0.2	13.100 54(2)	13.100 53
0.5	1.842 923(2)	1.842 850
1	0.154 188 6(2)	0.154 101 4
2	−0.206 200 84(7)	−0.206 219 38
5	−0.203 932 35(2)	−0.203 843 14
10	−0.142 869 097(9)	−0.142 781 622
15	−0.110 466 761(4)	−0.110 400 702
20	−0.090 777 768(2)	−0.090 727 757
50	−0.046 144(1)	−0.046 128
100	−0.026 699(1)	−0.026 694

The DMC data from r_s = 1 to 20 are taken from Ref 53. The rest is taken from Refs. 55,83,96. The statistical error is reported in parenthesis.
DMC, diffusion Monte Carlo.

ferromagnetic transition is sometimes called a Bloch transition.[140] Expanding the HF expression of the paramagnetic state around $\zeta = 0$ yields

$$e_{\mathrm{HF}}^{\mathrm{FF}}(r_s,\zeta) = e_{\mathrm{HF}}^{\mathrm{FF}}(r_s,0) + \zeta^2\left(\frac{D+2}{D^2}\frac{\varepsilon_{\mathrm{t}}}{r_s^2}+\frac{D+1}{2D^2}\frac{\varepsilon_{\mathrm{x}}}{r_s}\right)+O\left(\zeta^4\right), \quad (68)$$

and reveals that this state is locally stable with respect to partial spin polarization until

$$r_s^+ = -\frac{2(D+2)}{D+1}\frac{\varepsilon_t}{\varepsilon_x} = \begin{cases} 2.221, & D=2, \\ 6.029, & D=3. \end{cases} \quad (69)$$

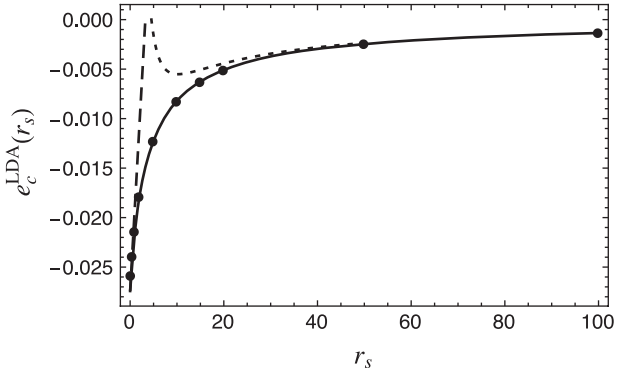

FIGURE 5 | $e_c^{LDA}(r_s)$ of 1-jellium given by Eq. (66a) as a function of r_s (solid line). Diffusion Monte Carlo results from Table 7 are shown by black dots. The small-r_s expansion of Eq. (49a) (dashed line) and large-r_s approximation of Eq. (60) (dotted line) are also shown.

The fact that $r_s^+ > r_s^{\mathrm{B}}$ implies that this state is locally stable with respect to partial spin polarization and will not undergo a continuous phase transition to the ferromagnetic state, in contrast to the predictions of DMC calculations on 3-jellium, as discussed in the *Quantum Monte Carlo* section.

For $r_s > r_s^{\mathrm{B}}$, the ferromagnetic state is lower in energy than the paramagnetic state. However, a similar stability analysis yields

$$e_{\mathrm{HF}}^{\mathrm{FF}}(r_s,\zeta) = e_{\mathrm{HF}}^{\mathrm{FF}}(r_s,1) - (1-\zeta)\left(\frac{D+2}{2^{\frac{D-1}{D}}D}\frac{\varepsilon_{\mathrm{t}}}{r_s^2}+\frac{D+1}{2^{\frac{D-1}{D}}D}\frac{\varepsilon_{\mathrm{x}}}{r_s}\right) + O\left((1-\zeta)^{\frac{D+1}{D}}\right), \quad (70)$$

which shows that the ferromagnetic state is never a stationary minimum. In fact, for $r_s < r_s^-$, where

$$r_s^- = \frac{r_s^+}{2^{\frac{D-1}{D}}} = \begin{cases} 1.571, & D=2, \\ 3.798, & D=3, \end{cases} \quad (71)$$

the ferromagnetic state is locally unstable and can undergo a continuous depolarization toward the paramagnetic state. Taken together, these predictions

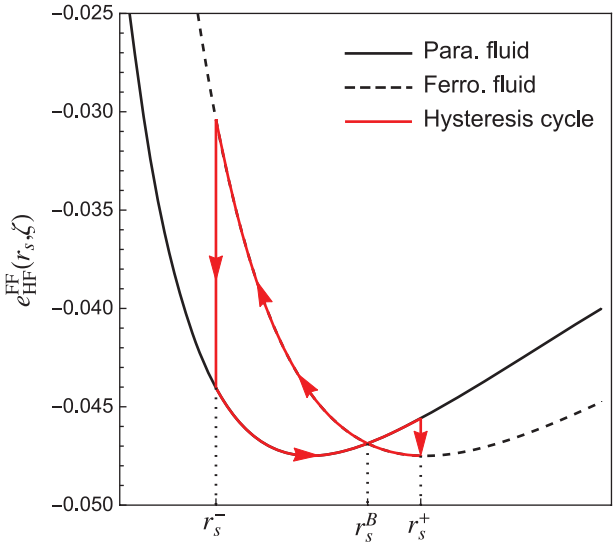

FIGURE 6 | $e_{HF}^{FF}(r_s,\zeta)$ as a function of r_s for the paramagnetic and ferromagnetic fluid phases of 3-jellium (see Eq. (18)). For $r_s > r_s^B$, the ferromagnetic fluid becomes lower in energy than the paramagnetic fluid (Bloch transition). For $r_s < r_s^-$, the ferromagnetic fluid becomes locally unstable toward depolarization, while for $r_s > r_s^+$, the paramagnetic fluid becomes locally unstable toward polarization. The 'hysteresis loop' is indicated in red.

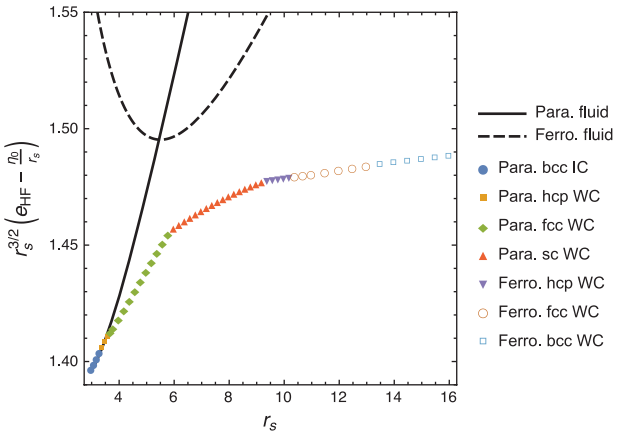

FIGURE 7 | SBHF phase diagram of 3-jellium constructed with the data of Refs 141 and 142, (see Table 8).

imply the 'hysteresis loop' shown in Figure 6 for 3-jellium.

3-jellium

Baguet et al.[141,142] have obtained what is thought to be the complete phase diagram of 3-jellium at the HF level. The SBHF phase diagram of 3-jellium is represented in Figure 7 using the data reported in Refs 141,142 (see Table 8). In addition to the usual FF and WC phases, they have also considered incommensurate crystals (ICs) with sc, fcc, bcc, and hcp unit cells. In an IC, the number of maxima of the charge density is higher than the number of electrons, having thus metallic character. As one can see in Figure 7, the phase diagram is complicated and, unfortunately, finite-size effects prevent a precise

TABLE 8 | SBHF Energy (in Millihartree) of 3-jellium for Various r_s Values

r_s	Energy	Lattice	Phase	Polarization	r_s	Energy	Lattice	Phase	Polarization
3.0	−29.954	bcc	IC	Para.	7.6	−47.804	sc	WC	Para.
3.1	−32.826	bcc	IC	Para.	7.8	−47.403	sc	WC	Para.
3.2	−35.289	bcc	IC	Para.	8.0	−46.992	sc	WC	Para.
3.3	−37.399	bcc	IC	Para.	8.2	−46.576	sc	WC	Para.
3.4	−39.287	hcp	WC	Para.	8.4	−46.155	sc	WC	Para.
3.5	−40.923	hcp	WC	Para.	8.6	−45.731	sc	WC	Para.
3.6	−42.437	hcp	WC	Para.	8.8	−45.307	sc	WC	Para.
3.7	−43.727	fcc	WC	Para.	9.0	−44.883	sc	WC	Para.
3.8	−44.899	fcc	WC	Para.	9.2	−44.461	sc	WC	Para.
4.0	−46.775	fcc	WC	Para.	9.4	−44.050	hcp	WC	Ferro.
4.2	−48.157	fcc	WC	Para.	9.6	−43.647	hcp	WC	Ferro.
4.4	−49.151	fcc	WC	Para.	9.8	−43.245	hcp	WC	Ferro.
4.6	−49.841	fcc	WC	Para.	10.0	−42.844	hcp	WC	Ferro.
4.8	−50.292	fcc	WC	Para.	10.2	−42.444	hcp	WC	Ferro.
5.0	−50.554	fcc	WC	Para.	10.4	−42.047	fcc	WC	Ferro.
5.2	−50.665	fcc	WC	Para.	10.7	−41.461	fcc	WC	Ferro.
5.4	−50.656	fcc	WC	Para.	11.0	−40.883	fcc	WC	Ferro.
5.6	−50.551	fcc	WC	Para.	11.5	−39.936	fcc	WC	Ferro.
5.8	−50.368	fcc	WC	Para.	12.0	−39.015	fcc	WC	Ferro.
6.0	−50.192	sc	WC	Para.	12.5	−38.126	fcc	WC	Ferro.
6.2	−50.031	sc	WC	Para.	13.0	−37.267	fcc	WC	Ferro.
6.4	−49.813	sc	WC	Para.	13.5	−36.441	bcc	WC	Ferro.
6.6	−49.550	sc	WC	Para.	14.0	−35.645	bcc	WC	Ferro.
6.8	−49.249	sc	WC	Para.	14.5	−34.880	bcc	WC	Ferro.
7.0	−48.919	sc	WC	Para.	15.0	−34.142	bcc	WC	Ferro.
7.2	−48.566	sc	WC	Para.	15.5	−33.432	bcc	WC	Ferro.
7.4	−48.193	sc	WC	Para.	16.0	−32.748	bcc	WC	Ferro.

The energy data are taken from the supplementary materials of Ref 141. The precision of the calculations is of the order 5×10^{-3} millihartree.
SBHF, symmetry-broken Hartree–Fock; bcc, body-centered cubic; fcc, face-centered cubic; hcp, hexagonal closed pack; IC, incommensurate crystal; sc, simple cubic; WC, Wigner crystal.

determination of the ground state for $r_s < 3$. However, extending the analysis of Ref 143, one can prove that the incommensurate phases are always energetically lower than the FF in the high-density limit. This particular point has been recently discussed in Ref 144.

For $3 < r_s < 3.4$, the incommensurate metallic phase with a bcc lattice is found to be the lowest-energy state. For $r_s > 3.4$, the 3-jellium ground state is a paramagnetic WC with hcp ($3.4 < r_s < 3.7$), fcc ($3.7 < r_s < 5.9$), and sc ($5.9 < r_s < 9.3$) lattices. From any value of r_s greater than 9.3, the ground state is a ferromagnetic WC with hcp ($9.3 < r_s < 10.3$), fcc ($10.3 < r_s < 13$), and finally bcc ($r_s > 13$) lattices. It is interesting to note that, compared to the DMC results from the *Quantum Monte Carlo* section, at the HF level, the Wigner crystallization happens at much higher densities, revealing a key deficiency of the HF theory.

2-jellium

In 2D, Bernu et al.[145] have obtained the SBHF phase diagram by considering the FF, the WC, and the IC with square or triangular lattices. The phase diagram is shown in Figure 8. They have shown that the incommensurate phase is always favored compared to the FF, independently of the imposed polarization and crystal symmetry, in agreement with the early prediction of Overhauser about the instability of the FF phase.[49,50] The paramagnetic incommensurate hexagonal crystal is the true HF ground state at high densities ($r_s < 1.22$). For $r_s > 1.22$, the paramagnetic incommensurate hexagonal crystal becomes a commensurate WC of hexagonal symmetry, and at $r_s \approx 1.6$, a structural transition from the paramagnetic hexagonal WC to the ferromagnetic square WC occurs, followed by a transition from the paramagnetic square WC to the ferromagnetic triangular WC at $r_s \approx 2.6$. Interestingly, as at the DMC level (see *Quantum Monte Carlo* section), they do not find a stable partially polarized state.

1-jellium

To the best of our knowledge, the SBHF phase diagram of 1-jellium is unknown, but it would probably be very instructive.

Finite-Temperature Calculations

All the results reported in the present review concerned the UEG at zero temperature. Recently, particular efforts have been devoted to obtain the properties of the finite-temperature UEG in the warm-dense regime using restricted path-integral

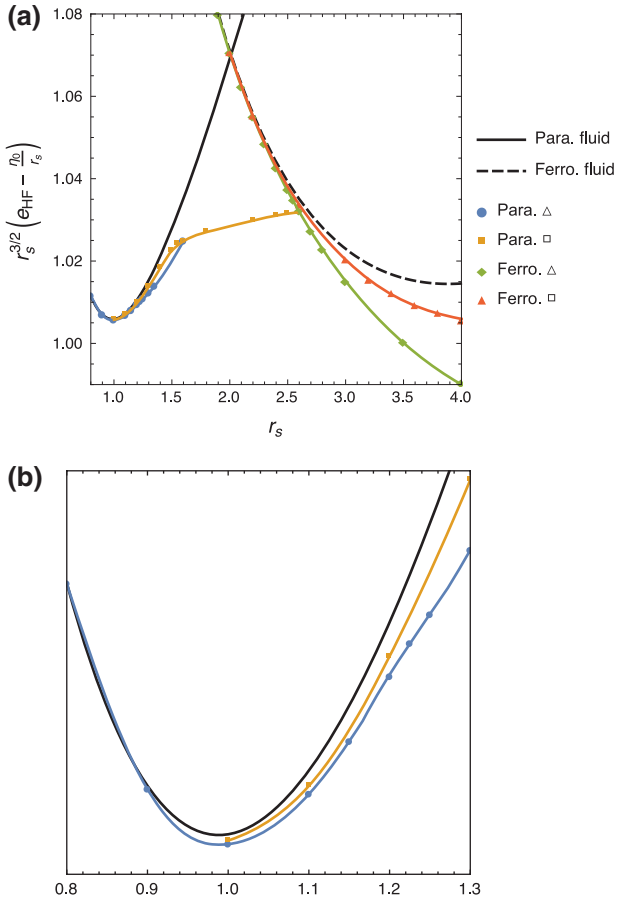

FIGURE 8 | Left: Symmetry-broken Hartree–Fock (SBHF) phase diagram of 2-jellium constructed with the data of Ref 145. Right: SBHF in the high-density region ($0 < r_s < 1.3$).

Monte Carlo calculations.[146–148] The finite-temperature UEG is of key relevance for many applications in dense plasmas, warm dense matter, and finite-temperature DFT.[149,150]

CONCLUSION

Mark Twain once wrote, 'There is something fascinating about science. One gets such wholesale returns of conjecture out of such a trifling investment of fact.' How true this is of the UEG! We have no simpler paradigm for the study of large numbers of interacting electrons and yet, out of that simplicity, behavior of such complexity emerges that the UEG has become one of the most powerful pathways for rationalizing and predicting the properties of atoms, molecules, and condensed-phase systems. The beauty of this unexpected *ex nihilo* complexity has lured many brilliant minds over the years and yet it is a

siren song for, 90 years after the publication of Schrödinger's equation, a complete understanding of the UEG (even in the nonrelativistic limit) continues to elude quantum scientists.

In this review, we have focused on the energy of the UEG, rather than on its many other interesting properties. We have done so partly for the sake of brevity and partly because most properties can be cast as derivatives of the energy with respect to one or more external parameters. Such properties are attracting increasing attention in their own right and we look forward to comprehensive reviews on these in the years ahead. However, we also foresee continued developments in the accurate calculations of the energies themselves. These will play a critical role in the ongoing evolution of QMC methodology and will improve our understanding of, and our ability to model, phase transitions in large quantum mechanical systems.

Many regard a full treatment of the UEG as one of the major unsolved problems in quantum science. We hope that, by providing a snapshot of the state of the art in 2016, we will inspire the next generation to roll up their sleeves and confront this fascinating challenge.

NOTE

[a] The difference between the crystallization densities reported in Refs 120 and 12 is less than two error bars, whereas the crystallization density difference between Refs 120 and 123 is of greater significance.

ACKNOWLEDGMENTS

The authors would like to thank Neil Drummond, Mike Towler, and John Trail for useful discussions, and Bernard Bernu and Lucas Baguet for providing the data for the phase diagram of 2-jellium. P.F.L. thanks the Australian Research Council for a Discovery Early Career Researcher Award (Grant No. DE130101441) and a Discovery Project grant (DP140104071). P.M.W.G. thanks the Australian Research Council for funding (Grants No. DP120104740 and DP140104071).

REFERENCES

1. Parr RG, Yang W. *Density-Functional Theory of Atoms and Molecules*. Oxford: Clarendon Press; 1989.
2. Kohn W. Nobel lecture: electronic structure of matter—wave functions and density functionals. *Rev Mod Phys* 1999, 71:1253–1266.
3. Pople JA. Nobel lecture: quantum chemical models. *Rev Mod Phys* 1999, 71:1267–1274.
4. Hohenberg P, Kohn W. Inhomogeneous electron gas. *Phys Rev* 1964, 136:B864–B871.
5. Giuliani GF, Vignale G. *Quantum Theory of the Electron Liquid*. Cambridge: Cambridge University Press; 2005.
6. Sommerfeld A. Zur elektronentheorie der metalle auf grund der fermischen statistik. *Zeits fur Physik* 1928, 47:1–32.
7. Kohn W, Sham LJ. Self-consistent equations including exchange and correlation effects. *Phys Rev* 1965, 140:A1133–A1138.
8. Vosko SH, Wilk L, Nusair M. Accurate spin-dependent electron liquid correlation energies for local spin density calculations: a critical analysis. *Can J Phys* 1980, 58:1200.
9. Perdew JP, McMullen ER, Zunger A. Density-functional theory of the correlation energy in atoms and ions: a simple analytic model and a challenge. *Phys Rev A* 1981, 23:2785–2789.
10. Perdew JP, Wang Y. Accurate and simple analytic representation of the electron-gas correlation energy. *Phys Rev B* 1992, 45:13244–13249.
11. Ceperley DM. Ground state of the fermion one-component plasma: a Monte Carlo study in two and three dimensions. *Phys Rev B* 1978, 18:3126–3138.
12. Ceperley DM, Alder BJ. Ground state of the electron gas by a stochastic method. *Phys Rev Lett* 1980, 45:566–569.
13. Huotari S, Soininen JA, Pylkkäanen T, Hämäläinen K, Issolah A, Titov A, McMinis J, Kim J, Esler K, Ceperley DM, et al. Momentum distribution and renormalization factor in sodium and the electron gas. *Phys Rev Lett* 2010, 105:086403.
14. Ando T, Fowler AB, Stern F. Electronic properties of two-dimensional systems. *Rev Mod Phys* 1982, 54:437–672.
15. Abrahams E, Kravchenko SV, Sarachik MP. Metallic behavior and related phenomena in two dimensions. *Rev Mod Phys* 2001, 73:251–266.
16. Alhassid Y. The statistical theory of quantum dots. *Rev Mod Phys* 2000, 72:895–968.
17. Reimann SM, Manninen M. Electronic structure of quantum dots. *Rev Mod Phys* 2002, 74:1283–1342.

18. Saito R, Dresselhauss G, Dresselhaus MS. *Properties of Carbon Nanotubes*. London: Imperial College Press; 1998.
19. Egger R, Gogolin AO. Correlated transport and non-Fermi-liquid behavior in single-wall carbon nanotubes. *Eur Phys J B* 1998, 3:281–300.
20. Bockrath M, Cobden DH, Lu J, Rinzler AG, Smalley RE, Balents L, McEuen PL. Luttinger-liquid behaviour in carbon nanotubes. *Nature* 1999, 397:598–601.
21. Ishii H, Kataura H, Shiozawa H, Yoshioka H, Otsubo H, Takayama Y, Miyahara T, Suzuki S, Achiba Y, Nakatake M, et al. Direct observation of Tomonaga–Luttinger-liquid state in carbon nanotubes at low temperatures. *Nature* 2003, 426:540–544.
22. Shiraishi M, Ata M. Tomonaga–Luttinger-liquid behavior in single-walled carbon nanotube networks. *Solid State Commun* 2003, 127:215–218.
23. Schwartz A, Dressel M, Grüuner G, Vescoli V, Degiorgi L, Giamarchi T. On-chain electrodynamics of metallic $(TMTSF)_2X$ salts: observation of Tomonaga–Luttinger liquid response. *Phys Rev B* 1998, 58:1261–1271.
24. Vescoli V, Zwick F, Henderson W, Degiorgi L, Grioni M, Gruner G, Montgomery LK. Optical and photoemission evidence for a Tomonaga–Luttinger liquid in the Bechgaard salts. *Eur Phys J B* 2000, 13:503–511.
25. Lorenz T, Hofmann M, Grüninger M, Freimuth A, Uhrig GS, Dumm M, Dressel M. Evidence for spin–charge separation in quasi-one-dimensional organic conductors. *Nature* 2002, 418:614–617.
26. Dressel M, Petukhov K, Salameh B, Zornoza P, Giamarchi T. Scaling behavior of the longitudinal and transverse transport in quasi-one-dimensional organic conductors. *Phys Rev B* 2005, 71:075104.
27. Ito T, Chainani A, Haruna T, Kanai K, Yokoya T, Shin S, Kato R. Temperature-dependent Luttinger surfaces. *Phys Rev Lett* 2005, 95:246402.
28. Hu Z, Knupfer M, Kielwein M, RoÏer UK, Golden MS, Fink J, de Groot FMF, Ito T, Oka K, Kaindl G. The electronic structure of the doped one-dimensional transition metal oxide Y2-xCaxBaNiO5 studied using X-ray absorption. *Eur Phys J B* 2002, 26:449–453.
29. Milliken FP, Umbach CP, Webb RA. Indications of a Luttinger liquid in the fractional quantum Hall regime. *Solid State Commun* 1996, 97:309–313.
30. Mandal SS, Jain JK. How universal is the fractional-quantum-Hall edge Luttinger liquid? *Solid State Commun* 2001, 118:503–507.
31. Chang AM. Chiral Luttinger liquids at the fractional quantum Hall edge. *Rev Mod Phys* 2003, 75:1449–1505.
32. Gonï AR, Pinczuk A, Weiner JS, Calleja JM, Dennis BS, Pfeiffer LN, West KW. One-dimensional plasmon dispersion and dispersionless intersubband excitations in gaas quantum wires. *Phys Rev Lett* 1991, 67:3298–3301.
33. Auslaender OM, Yacoby A, dePicciotto R, Baldwin KW, Pfeiffer LN, West KW. Experimental evidence for resonant tunneling in a Luttinger liquid. *Phys Rev Lett* 2000, 84:1764–1767.
34. Zaitsev-Zotov SV, Kumzerov YA, Firsov YA, Monceau P. Luttinger-liquid-like transport in long InSb nanowires. *J Phys Condens Matter* 2000, 12: L303–L309.
35. Liu F, Bao M, Wang KL, Li C, Lei B, Zhou C. One-dimensional transport of In_2O_3 nanowires. *Appl Phys Lett* 2005, 86:213101.
36. Steinberg H, Auslaender OM, Yacoby A, Qian J, Fiete GA, Tserkovnyak Y, Halperin BI, Baldwin KW, Pfeiffer LN, West KW. Localization transition in a ballistic quantum wire. *Phys Rev B* 2006, 73:113307.
37. Monien H, Linn M, Elstner N. Trapped one-dimensional Bose gas as a Luttinger liquid. *Phys Rev A* 1998, 58:R3395–R3398.
38. Recati A, Fedichev PO, Zwerger W, Zoller P. Fermi one-dimensional quantum gas: Luttinger liquid approach and spin–charge separation. *J Opt B Quantum Semiclassical Opt* 2003, 5:S55–S64.
39. Moritz H, Stoferle T, Guenter K, Kohl M, Esslinger T. Confinement induced molecules in a 1D Fermi gas. *Phys Rev Lett* 2005, 94:210401.
40. Schäafer J, Blumenstein C, Meyer S, Wisniewski M, Claessen R. New model system for a one-dimensional electron liquid: self-organized atomic gold chains on Ge(001). *Phys Rev Lett* 2008, 101:236802.
41. Huang Y, Duan X, Cui Y, Lauhon LJ, Kim K-H, Lieber CM. Logic gates and computation from assembled nanowire building blocks. *Science* 2001, 294:1313–1317.
42. Olver FWJ, Lozier DW, Boisvert RF, Clark CW, eds. *NIST Handbook of Mathematical Functions*. New York: Cambridge University Press; 2010.
43. Thomas LH. The calculation of atomic fields. *Proc Camb Philos Soc* 1927, 23:542–548.
44. Fermi E. Un metodo statistico per la determinazione di alcune priopriet a dell'atomo. *Rend Accad Naz Lincei* 1927, 6:602–607.
45. Glasser ML, Boersma J. Exchange energy of an electron gas of arbitrary dimensionality. *SIAM J Appl Math* 1983, 43:535–545.
46. Iwamoto N. Sum rules and static local-field corrections of electron liquids in two and three dimensions. *Phys Rev A* 1984, 30:3289–3304.
47. Dirac PAM. Note on exchange phenomena in the Thomas–Fermi atom. *Proc Camb Philos Soc* 1930, 26:376–385.

48. Friesecke G. Pair correlations and exchange phenomena in the free electron gas. *Commun Math Phys* 1997, 184:143–171.
49. Overhauser AW. New mechanism of antiferromagnetism. *Phys Rev Lett* 1959, 3:414–416.
50. Overhauser AW. Spin density waves in an electron gas. *Phys Rev* 1962, 128:1437–1452.
51. Fogler MM. Ground-state energy of the electron liquid in ultrathin wires. *Phys Rev Lett* 2005, 94:056405.
52. Astrakharchik GE, Girardeau MD. Exact ground-state properties of a one-dimensional Coulomb gas. *Phys Rev B* 2011, 83:153303.
53. Lee RM, Drummond ND. Ground-state properties of the one-dimensional electron liquid. *Phys Rev B* 2011, 83:245114.
54. Loos PF, Gill PMW. Exact wave functions of two-electron quantum rings. *Phys Rev Lett* 2012, 108:083002.
55. Loos PF, Gill PMW. Uniform electron gases. I. Electrons on a ring. *J Chem Phys* 2013, 138:164124.
56. Loos PF, Ball CJ, Gill PMW. Uniform electron gases. II. The generalized local density approximation in one dimension. *J Chem Phys* 2014, 140:18A524.
57. Loos PF, Ball CJ, Gill PMW. Chemistry in one dimension. *Phys Chem Chem Phys* 2015, 17:3196–3206.
58. Hoffman GG. Correlation energy of a spin-polarized electron gas at high density. *Phys Rev B* 1992, 45:8730–8733.
59. Zia RKP. Electron correlation in a high density gas confined to very thin films. *J Phys C* 1973, 6:3121–3129.
60. Isihara A, Toyoda T. Correlation energy of 2-D electrons. *Ann Phys* 1977, 106:394–406.
61. Rajagopal AK, Kimball JC. Correlations in a two-dimensional electron system. *Phys Rev B* 1977, 15:2819–2825.
62. Glasser ML. Pair correlation function for a two-dimensional electron gas. *J Phys C: Solid State Phys* 1977, 10:L121–L123.
63. Isihara A, Ioriatti L. Exact evaluation of the second-order exchange energy of a two-dimensional electron fluid. *Phys Rev B* 1980, 22:214–219.
64. Glasser ML. On some integrals arising in mathematical physics. *J Comp App Math* 1984, 10:293–299.
65. Seidl M. Spin-resolved second-order correlation energy of the two-dimensional uniform electron gas. *Phys Rev B* 2004, 70:073101.
66. Chesi S, Giuliani GF. Correlation energy in a spin-polarized two-dimensional electron liquid in the high-density limit. *Phys Rev B* 2007, 75:153306.
67. Loos PF, Gill PMW. Exact energy of the spin-polarized two-dimensional electron gas at high density. *Phys Rev B* 2011, 83:233102.
68. Macke W. Uber die wechselwirkungen im Fermi-gas. *Z Naturforsch A* 1950, 5a:192–208.
69. Bohm D, Pines D. A collective description of electron interactions: III. Coulomb interactions in a degenerate electron gas. *Phys Rev* 1953, 92:609–625.
70. Pines D. A collective description of electron interactions: IV. Electron interaction in metals. *Phys Rev* 1953, 92:626–636.
71. Gell-Mann M, Brueckner KA. Correlation energy of an electron gas at high density. *Phys Rev* 1957, 106:364–368.
72. DuBois DF. Electron interactions. Part I. Field theory of a degenerate electron gas. *Ann Phys* 1959, 7:174–237.
73. Carr WJ, Maradudin AA. Ground-state energy of a high-density electron gas. *Phys Rev* 1964, 133: A371–A374.
74. Misawa S. Ferromagnetism of an electron gas. *Phys Rev* 1965, 140:A1645–A1648.
75. Onsager L, Mittag L, Stephen MJ. Integrals in the theory of electron correlations. *Ann Phys* 1966, 18:71–77.
76. Wang Y, Perdew JP. Spin scaling of the electron-gas correlation energy in the high-density limit. *Phys Rev B* 1991, 43:8911–8916.
77. Endo T, Horiuchi M, Takada Y, Yasuhara H. High-density expansion of correlation energy and its extrapolation to the metallic density region. *Phys Rev B* 1999, 59:7367–7372.
78. Ziesche P, Cioslowski J. The three-dimensional electron gas at the weak-correlation limit: how peculiarities of the momentum distribution and the static structure factor give rise to logarithmic non-analyticities in the kinetic and potential correlation energies. *Physica A* 2005, 356:598–608.
79. Sun J, Perdew JP, Seidl M. Correlation energy of the uniform electron gas from an interpolation between high- and low-density limits. *Phys Rev B* 2010, 81:085123.
80. Loos PF, Gill PMW. Correlation energy of the spin-polarized uniform electron gas at high density. *Phys Rev B* 2011, 84:033103.
81. Loos PF, Gill PMW. Leading-order behavior of the correlation energy in the uniform electron gas. *Int J Quantum Chem* 2012, 112:1712–1716.
82. Loos P-F, Gill PMW. Thinking outside the box: the uniform electron gas on a hypersphere. *J Chem Phys* 2011, 135:214111.
83. Loos PF. High-density correlation energy expansion of the one-dimensional uniform electron gas. *J Chem Phys* 2013, 138:064108.
84. Wolfram Research, Inc.. *Mathematica* 7. 2008.

85. Loos PF. unpublished.
86. Gill PMW, Loos PF, Agboola D. Basis functions for electronic structure calculations on spheres. *J Chem Phys* 2014, 141:244102.
87. Agboola D, Knol AL, Gill PMW, Loos PF. Uniform electron gases. III. Low-density gases on three-dimensional spheres. *J Chem Phys* 2015, 143:084114.
88. Wigner E. On the interaction of electrons in metals. *Phys Rev* 1934, 46:1002–1011.
89. Loos PF, Gill PMW. Ground state of two electrons on a sphere. *Phys Rev A* 2009, 79:062517.
90. Aguilera-Navarro VC, Baker GA Jr, de Llano M. Ground-state energy of jellium. *Phys Rev B* 1985, 32:4502–4506.
91. Fuchs K. A quantum mechanical investigation of the cohesive forces of metallic copper. *Proc R Soc* 1935, 151:585–602.
92. Carr WJ Jr. Energy, specific heat, and magnetic properties of the low-density electron gas. *Phys Rev* 1961, 122:1437–1446.
93. Kohn W, Schechter D. unpublished. 1961.
94. Carr WJ Jr, Coldwell-Horsfall RA, Fein AE. Anharmonic contribution to the energy of a dilute electron gas: interpolation for the correlation energy. *Phys Rev* 1961, 124:747–752.
95. Bonsall L, Maradudin AA. Some static and dynamical properties of a two-dimensional Wigner crystal. *Phys Rev B* 1977, 15:1959–1973.
96. Loos PF. Generalized local-density approximation and one-dimensional finite uniform 34 electron gases. *Phys Rev A* 2014, 89:052523.
97. Foulkes WMC, Mitas L, Needs RJ, Rajagopal G. Quantum Monte Carlo simulations of solids. *Rev Mod Phys* 2001, 73:33–83.
98. Kolorenc J, Mitas L. Applications of quantum Monte Carlo methods in condensed systems. *Rep Prog Phys* 2011, 74:026502.
99. Fraser LM, Foulkes WMC, Rajagopal G, Needs RJ, Kenny SD, Williamson AJ. Finite-size effects and coulomb interactions in quantum Monte Carlo calculations for homogeneous systems with periodic boundary conditions. *Phys Rev B* 1996, 53:1814–1832.
100. Lin C, Zong FH, Ceperley DM. Twist-averaged boundary conditions in continuum quantum Monte Carlo algorithms. *Phys Rev E* 2001, 64:016702.
101. Kwee H, Zhang S, Krakauer H. Finite-size correction in many-body electronic structure calculations. *Phys Rev Lett* 2008, 100:126404.
102. Drummond ND, Needs RJ, Sorouri A, Foulkes WMC. Finite-size errors in continuum quantum Monte Carlo calculations. *Phys Rev B* 2008, 78:125106.
103. Ma F, Zhang S, Krakauer H. Finite-size correction in many-body electronic structure calculations of magnetic systems. *Phys Rev B* 2011, 84:155130.
104. Ceperley DM. Fermion nodes. *J Stat Phys* 1991, 63:1237–1267.
105. Bressanini D, Ceperley DM, Reynolds P. What do we know about wave function nodes? In: Lester WA Jr, Rothstein SM, Tanaka S, eds. *Recent Advances in Quantum Monte Carlo Methods*, vol. 2. Singapore: World Scientfic; 2001, 3–11.
106. Bajdich M, Mitas L, Drobny G, Wagner LK. Approximate and exact nodes of fermionic wavefunctions: coordinate transformations and topologies. *Phys Rev B* 2005, 72:075131.
107. Bressanini D, Reynolds PJ. Unexpected symmetry in the nodal structure of the He atom. *Phys Rev Lett* 2005, 95:110201.
108. Bressanini D, Morosi G, Tarasco S. An investigation of nodal structures and the construction of trial wave functions. *J Chem Phys* 2005, 123:204109.
109. Mitas L. Structure of fermion nodes and nodal cells. *Phys Rev Lett* 2006, 96:240402.
110. Scott TC, Luchow A, Bressanini D, Morgan JD III. Nodal surfaces of helium atom eigenfunctions. *Phys Rev A* 2007, 75:060101.
111. Bressanini D, Morosi G. On the nodal structure of single-particle approximation based atomic wave functions. *J Chem Phys* 2008, 129:054103.
112. Mitas L. Fermion nodes and nodal cells of noninteracting and interacting fermions. arXiv:cond-mat:/0605550. 2008.
113. Bressanini D. Implications of the two nodal domains conjecture for ground state fermionic wave functions. *Phys Rev B* 2012, 86:115120.
114. Rasch KM, Mitas L. Impact of electron density on the fixed-node errors in quantum Monte Carlo of atomic systems. *Chem Phys Lett* 2012, 528:59–62.
115. Kulahlioglu AH, Rasch KM, Hu S, Mitas L. Density dependence of fixed-node errors in diffusion quantum Monte Carlo: triplet pair correlations. *Chem Phys Lett* 2014, 591:170–174.
116. Rasch KM, Hu S, Mitas L. Fixed-node errors in quantum Monte Carlo: interplay of electron density and node nonlinearities. *J Chem Phys* 2014, 140:041102.
117. Loos PF, Bressanini D. Nodal surfaces and interdimensional degeneracies. *J Chem Phys* 2015, 142:214112.
118. Ortiz G, Ballone P. Correlation energy, structure factor, radial distribution function, and momentum distribution of the spin-polarized uniform electron gas. *Phys Rev B* 1994, 50:1391–1405.
119. Ortiz G, Ballone P. Erratum: Correlation energy, structure factor, radial distribution function, and momentum distribution of the spin-polarized uniform

electron gas [Phys. Rev. B 50, 1391 (1994)]. *Phys Rev B* 1997, 56:9970.

120. Ortiz G, Harris M, Ballone P. Zero temperature phases of the electron gas. *Phys Rev Lett* 1999, 82:5317–5320.
121. Kwon Y, Ceperley DM, Martin RM. Effects of backflow correlation in the three-dimensional electron gas: quantum Monte Carlo study. *Phys Rev B* 1998, 58:6800–6806.
122. Zong FH, Lin C, Ceperley DM. Spin polarization of the low-density three-dimensional electron gas. *Phys Rev E* 2002, 66:036703.
123. Drummond ND, Towler MD, Needs RJ. Jastrow correlation factor for atoms, molecules, and solids. *Phys Rev B* 2004, 70:235119.
124. Spink GG, Needs RJ, Drummond ND. Quantum Monte Carlo study of the three-dimensional spin-polarized homogeneous electron gas. *Phys Rev B* 2013, 88:085121.
125. Tanatar B, Ceperley DM. Ground state of the two-dimensional electron gas. *Phys Rev B* 1989, 39:5005–5016.
126. Kwon Y, Ceperley DM, Martin RM. Effects of three-body and backflow correlations in the two-dimensional electron gas. *Phys Rev B* 1993, 48:12037–12046.
127. Rapisarda F, Senatore G. Diffusion Monte Carlo study of electrons in two-dimensional layers. *Aust J Phys* 1996, 49:161–182.
128. Attaccalite C, Moroni S, Gori-Giorgi P, Bachelet GB. Correlation energy and spin polarization in the 2D electron gas. *Phys Rev Lett* 2002, 88:256601.
129. Attaccalite C, Moroni S, Gori-Giorgi P, Bachelet GB. Erratum: Correlation energy and spin polarization in the 2D electron gas [Phys. Rev. Lett. 88, 256601 (2002)]. *Phys Rev Lett* 2003, 91:109902.
130. Gori-Giorgi P, Attaccalite C, Moroni S, Bachelet GB. Two-dimensional electron gas: correlation energy versus density and spin polarization. *Int J Quantum Chem* 2003, 91:126–130.
131. Drummond ND, Needs RJ. Phase diagram of the low-density two-dimensional homogeneous electron gas. *Phys Rev Lett* 2009, 102:126402.
132. Spivak B, Kivelson SA. Phases intermediate between a two-dimensional electron liquid and Wigner crystal. *Phys Rev B* 2004, 70:155114.
133. Falakshahi H, Waintal X. Hybrid phase at the quantum melting of the Wigner crystal. *Phys Rev Lett* 2005, 94:046801.
134. Waintal X. On the quantum melting of the two-dimensional Wigner crystal. *Phys Rev B* 2006, 73:075417.
135. Clark BK, Casula M, Ceperley DM. Hexatic and mesoscopic phases in a 2D quantum Coulomb system. *Phys Rev Lett* 2009, 103:055701.
136. Cioslowski J, Strasburger K, Matito E. The three-electron harmonium atom: the lowest-energy doublet and quadruplet states. *J Chem Phys* 2012, 136:194112.
137. Zhang S, Ceperley DM. Hartree-Fock ground state of the three-dimensional electron gas. *Phys Rev Lett* 2008, 100:236404.
138. Bernu B, Delyon F, Duneau M, Holzmann M. Metal-insulator transition in the 37 Hartree-Fock phase diagram of the fully polarized homogeneous electron gas in two dimensions. *Phys Rev B* 2008, 78:245110.
139. Trail JR, Towler MD, Needs RJ. Unrestricted Hartree-Fock theory of Wigner crystals. *Phys Rev B* 2003, 68:045107.
140. Bloch Z. Bemerkung zur elektronentheorie des ferromagnetismus und der elektrischen leitfähigkeit. *Z Physik* 1929, 57:545–555.
141. Baguet L, Delyon F, Bernu B, Holzmann M. Hartree-Fock ground state phase diagram of jellium. *Phys Rev Lett* 2013, 111:166402.
142. Baguet L, Delyon F, Bernu B, Holzmann M. Properties of Hartree-Fock solutions of the three-dimensional electron gas. *Phys Rev B* 2014, 90:165131.
143. Delyon F, Duneau M, Bernu B, Holzmann M. Existence of a metallic phase and upper bounds of the Hartree-Fock energy in the homogeneous electron gas. arXiv:0807.0770v1. 2008.
144. Delyon F, Bernu B, Baguet L, Holzmann M. Upper bounds of spin-density wave energies in the homogeneous electron gas. *Phys Rev B* 2015, 92:235124.
145. Bernu B, Delyon F, Holzmann M, Baguet L. Hartree-Fock phase diagram of the two-dimensional electron gas. *Phys Rev B* 2011, 84:115115.
146. Brown EW, Clark BK, DuBois JL, Ceperley DM. Path-integral Monte Carlo simulation of the warm dense homogeneous electron gas. *Phys Rev Lett* 2013, 110:146405.
147. Filinov VS, Fortov VE, Bonitz M, Moldabekov Z. Fermionic path-integral Monte Carlo results for the uniform electron gas at finite temperature. *Phys Rev E* 2015, 91:033108.
148. Schoof T, Groth S, Vorberger J, Bonitz M. Ab initio thermodynamic results for the degenerate electron gas at finite temperature. *Phys Rev Lett* 2015, 115:130402.
149. Brown EW, DuBois JL, Holzmann M, Ceperley DM. Exchange-correlation energy for the three-dimensional homogeneous electron gas at arbitrary temperature. *Phys Rev B* 2013, 88:081102(R).
150. Brown EW, DuBois JL, Holzmann M, Ceperley DM. Erratum: Exchange correlation energy for the three-dimensional homogeneous electron gas at arbitrary temperature [Phys. Rev. B 88, 081102(R) (2013)]. *Phys Rev B* 2013, 88:199901.

